Shen et al., http://www.jcb.org/cgi/content/full/jcb.201403108/DC1

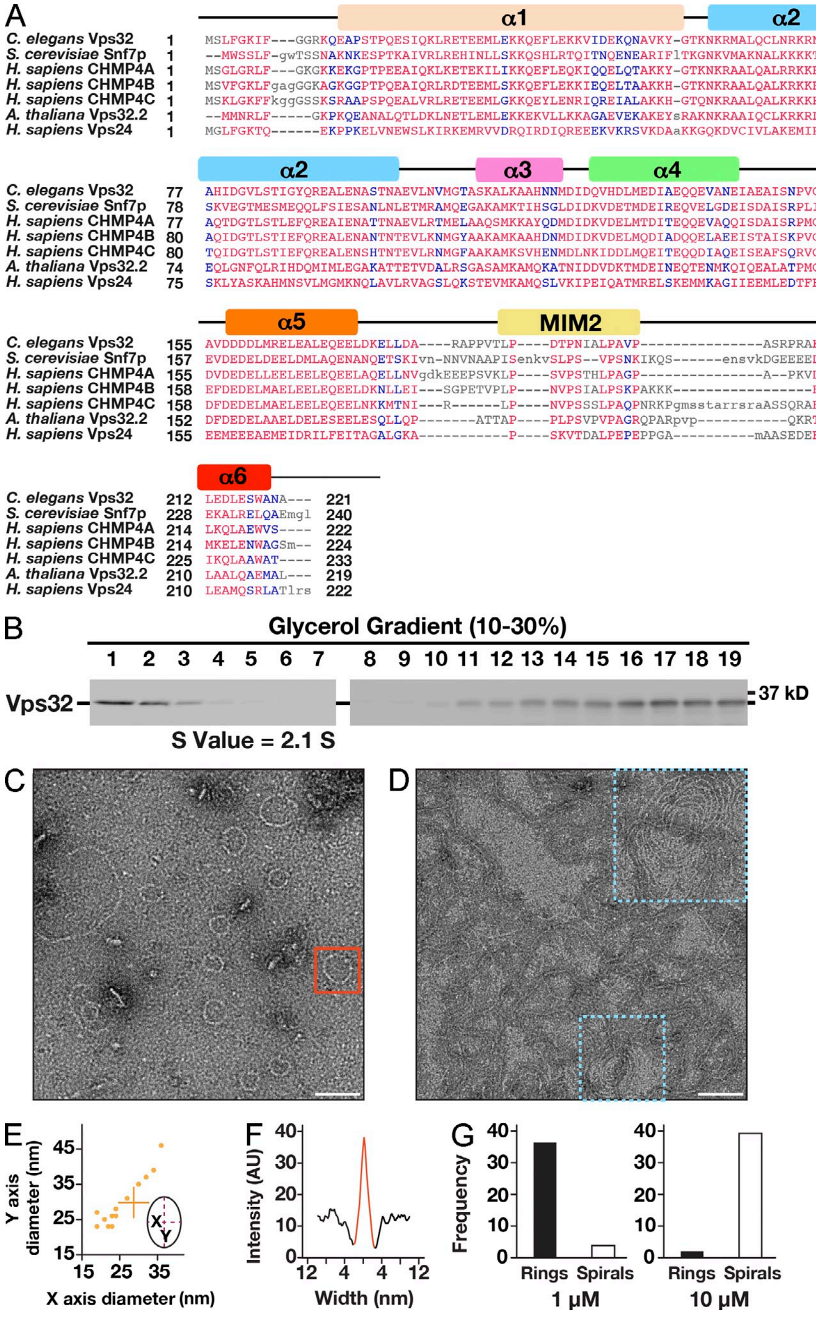

Figure S1. ***C. elegans*** **Vps32 is evolutionarily conserved and forms single-stranded circular filaments after negative straining EM.** (A) Sequence alignment of several ESCRT-III subunits from different species. The positions of helices α1–α6 and the MIT-interacting motif 2 (MIM2) domain are labeled. Red highlights conserved residues, blue highlights sequences with no gaps, and gray highlights sequences containing gaps. (B) Immunoblot analysis using α-Vps32 antibodies showing the distribution of recombinant Vps32 after fractionation over a glycerol density gradient. The first peak exhibits an approximate sedimentation value of 2.1 S, based on the elution profile of standards run in parallel. The remainder of Vps32 is found largely near the bottom of the gradient, preventing an accurate calculation of its sedimentation value. (C) A representative negatively stained EM image of purified, recombinant *C. elegans* Vps32 (1 µM). A Vps32 ring structure is highlighted (red boxed region). (D) A representative negatively stained EM image of purified, recombinant *C. elegans* Vps32 (10 µM). Vps32 spirals are highlighted (blue boxed regions). (E) Distribution of ring structure diameters. Both the innermost and outermost diameters of ringlike filaments were measured in two axes (x and y). Data shown are from multiple experiments, repeated at least four times independently. (F) A canonical ring structure (red boxed region in C) was chosen for further analysis to determine the width of Vps32 filaments (intensity after background subtraction was used to calculate the width of filaments). The data shown are from a single representative experiment, which was repeated three times ($n = 15$ for the experiment shown). AU, arbitrary unit. (G) Frequency distribution of ring structures and spiral polymers at different Vps32 concentrations. Only closed filaments were deemed as rings. Data shown are from multiple experiments, repeated at least three times independently. Bars, 50 nm.

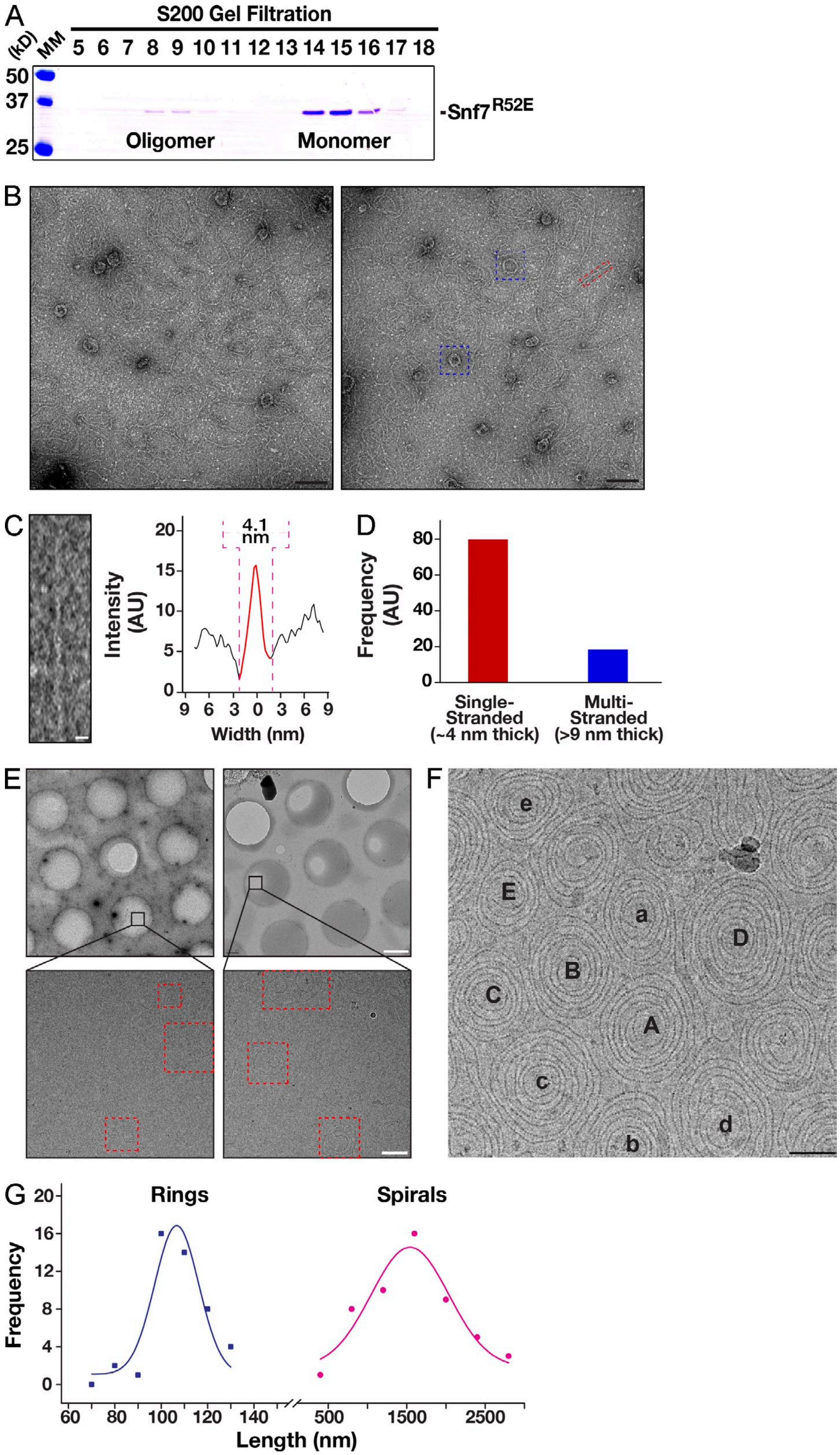

Figure S2. **Vps32 polymers form spiral filaments when observed in vitreous ice.** (A) Coomassie-stained fractions of purified, recombinant *S. cerevisiae* Snf7$^{\mathrm{R52E}}$ after size exclusion chromatography and SDS-PAGE analysis. The monomer and oligomer peaks are highlighted. MM, molecular mass. (B) Representative negatively stained EM images of purified, recombinant *S. cerevisiae* Snf7$^{\mathrm{R52E}}$ (4 µM). Bars, 50 nm. (C) A straight single-stranded filament (red boxed region in B) was selected for width analysis (intensity after background subtraction was used to calculate the width of filaments). Bar, 5 nm. The data shown are from a single representative experiment, which was repeated three times (n = 15 for the experiment shown). (D) Frequency distribution of single-stranded (e.g., red boxed filament in B) and multistranded polymers (e.g., blue boxed structures in B) composed of Snf7$^{\mathrm{R52E}}$. The frequency is defined by the total number of monomeric units per structure. Filament lengths were calculated based on our trajectory analysis. At least four different fields of view were considered to generate the frequency distribution. (E) Visibility of Vps32 spirals depends on the ice thickness. Although circular Vps32 filaments are present under thick ice (left) and thin ice (right), contrast is improved in the presence of thin ice. Representative filaments are highlighted (red boxed regions). Bars: (top) 1 µm; (bottom) 100 nm. (F) Higher magnification of Vps32 spiral pairs after cryo-EM. Select spiral pairs are marked with corresponding capital and lowercase letters. Bar, 50 nm. (G) A histogram showing the distribution of lengths observed for vitrified Vps32 rings (n = 45) and spirals (n = 52) is provided. The blue line highlights the frequency distribution of ringlike structures, and the red line highlights the frequency distribution of spiral structures. AU, arbitrary unit.

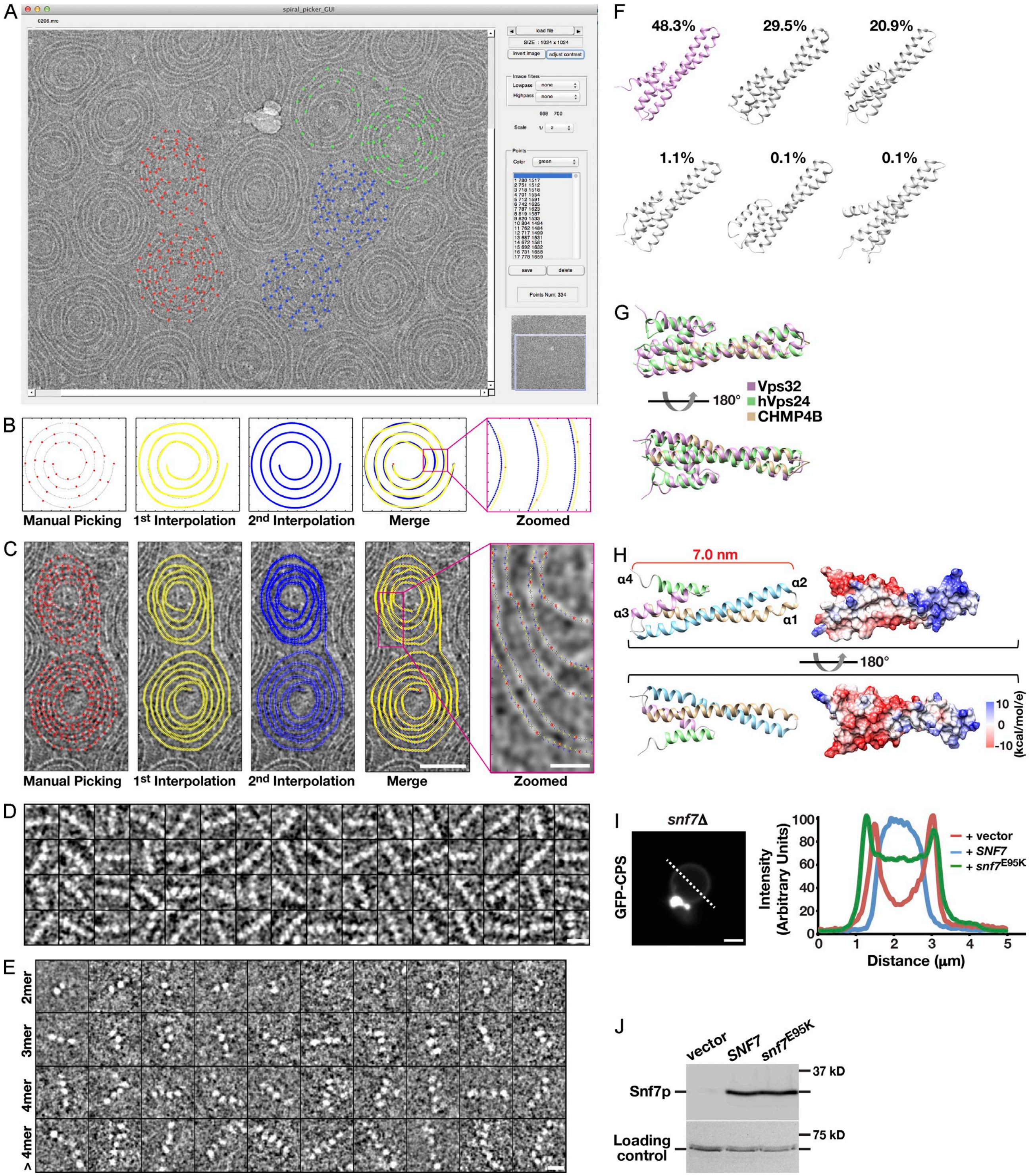

Figure S3. **Vps32 filaments are composed of distinct, globular densities joined by thin connections.** (A) Screenshot of GUI interface highlighting its multifunctionality. (B) Testing of the GUI system. A simulated spiral was marked aberrantly (manually) and analyzed. After two rounds of interpolation, an accurate trajectory was identified, as observed in the merged image (right). (C) An experimental spiral was marked, and the trajectory was defined after two rounds of interpolation. Bars: (left) 50 nm; (right zoomed image) 10 nm. (D) A montage of raw boxed datasets (inverted and low pass filtered) used for two-dimensional class average analysis of Vps32 polymers. Bar, 5 nm. (E) Raw EM density maps for representative Vps32 polymers of particular lengths. All particles shown were selected from inverted cryo-EM images. Bar, 5 nm. (F) Representative pseudoatomic structures of Vps32 obtained from MD simulations. Structures shown were obtained from cluster analysis of the 3 μs GB7 MD simulation trajectory, and the frequency of each cluster is indicated. A highly represented structure (purple) was selected as the initial model for further analysis. The initial structure was built using I-TASSER, which used crystal structures of both human Vps24 and CHMP4B as templates. (G) Superimposed structures of *C. elegans* Vps32, human Vps24, and human CHMP4B are shown, highlighting similarities in the helical hairpin of all proteins. (H) The modeled structure of *C. elegans* Vps32 (helices α1–α4) exhibits a length of $\sim$7 nm, and its surface electrostatic distribution is shown (two different views; negatively charged areas are indicated by red, and positively charged areas are highlighted in blue). (I) Line scan analysis (an example region is shown on the left as a dashed white line across a vacuole in a yeast cell lacking *SNF7*) highlights the defect in GFP-CPS sorting in cells expressing only *snf7*^{E95K}. Mutant *snf7*Δ cells expressing wild-type *SNF7* exhibit a homogenous distribution of GFP-CPS within the vacuole lumen. In contrast, cells lacking *SNF7* or expressing *snf7*^{E95K} in the *snf7*Δ genetic background accumulate GFP-CPS on the vacuole-limiting membrane. Data shown are representative of the population (>30 cells analyzed per condition). Bar, 1 μm. (J) Immunoblot analysis using anti-Snf7 antibodies (a gift from D. Katzmann) shows the levels of Snf7p expressed in *snf7*Δ mutant cells transformed with an empty vector, a vector expressing wild-type *SNF7*, or a vector expressing *snf7*^{E95K}.

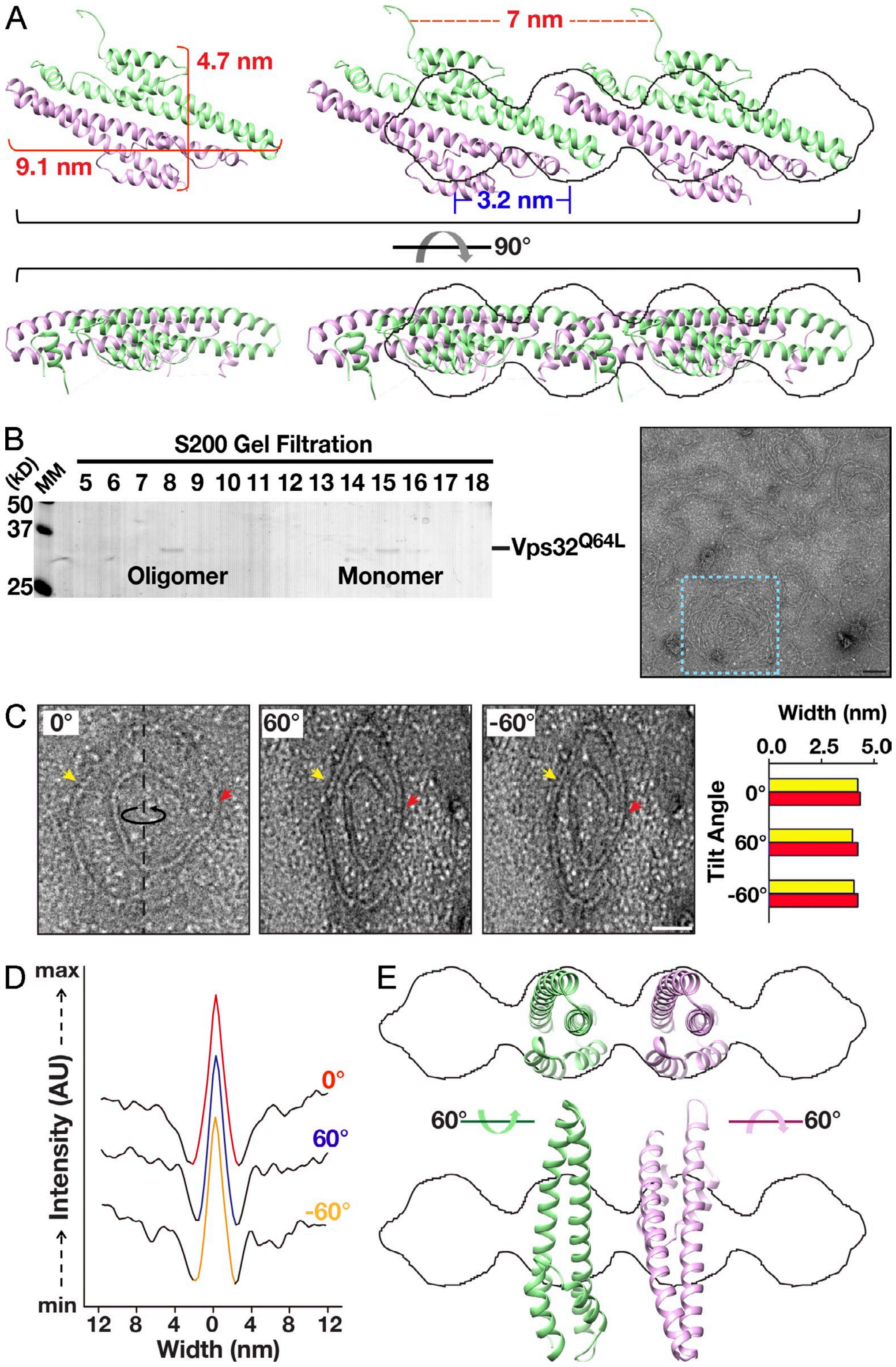

Figure S4. **Only a single orientation of Vps32 is compatible with the EM density map.** (A) Docking results for the human Vps24 dimer that was solved crystallographically (Muzioł et al., 2006) into the two-dimensional EM isosurface. In both end-on (top) and side (bottom) views, the dimer model fails to fit into the isosurface. Side views represent the possible curvature-forming orientation proposed previously (Muzioł et al., 2006). The dimensions of the human Vps24 dimer and the distance between dimers are marked (red). The repeating distance in the EM isosurface is also indicated (blue). (B) Coomassie-stained fractions of purified, recombinant Vps32^{Q64L} after size exclusion chromatography and SDS-PAGE analysis. The monomer and oligomer peaks are highlighted. On the right is a representative negatively stained EM image of purified, recombinant Vps32^{Q64L}. The blue boxed region highlights a representative spiral structure formed by Vps32^{Q64L}. MM, molecular mass. Bar, 50 nm. (C) A representative negatively stained Vps32 spiral filament and its respective ±60° tilted views are shown. Arrows highlight portions of the filament that are parallel to the tilting axis, and widths at these locations are indicated for all tilt angles (right). Bar, 25 nm. The data shown are from a single representative experiment, which was repeated two times (*n* = 5 for the experiment shown). (D) The mean thicknesses of Vps32 single-stranded filaments at different tilting angles. Curved filaments were first straightened and subsequently projected vertically to determine filament width. Plots at each angle specified are staggered relative to one another (intensity used for width analysis is provided in arbitrary units). The data shown are from a single representative experiment, which was repeated two times (*n* = 5 for the experiment shown). (E) The alternative orientation of Vps32 that docks into the isosurface map at one angle fails to be compatible with the density map at other tilt angles. AU, arbitrary unit.

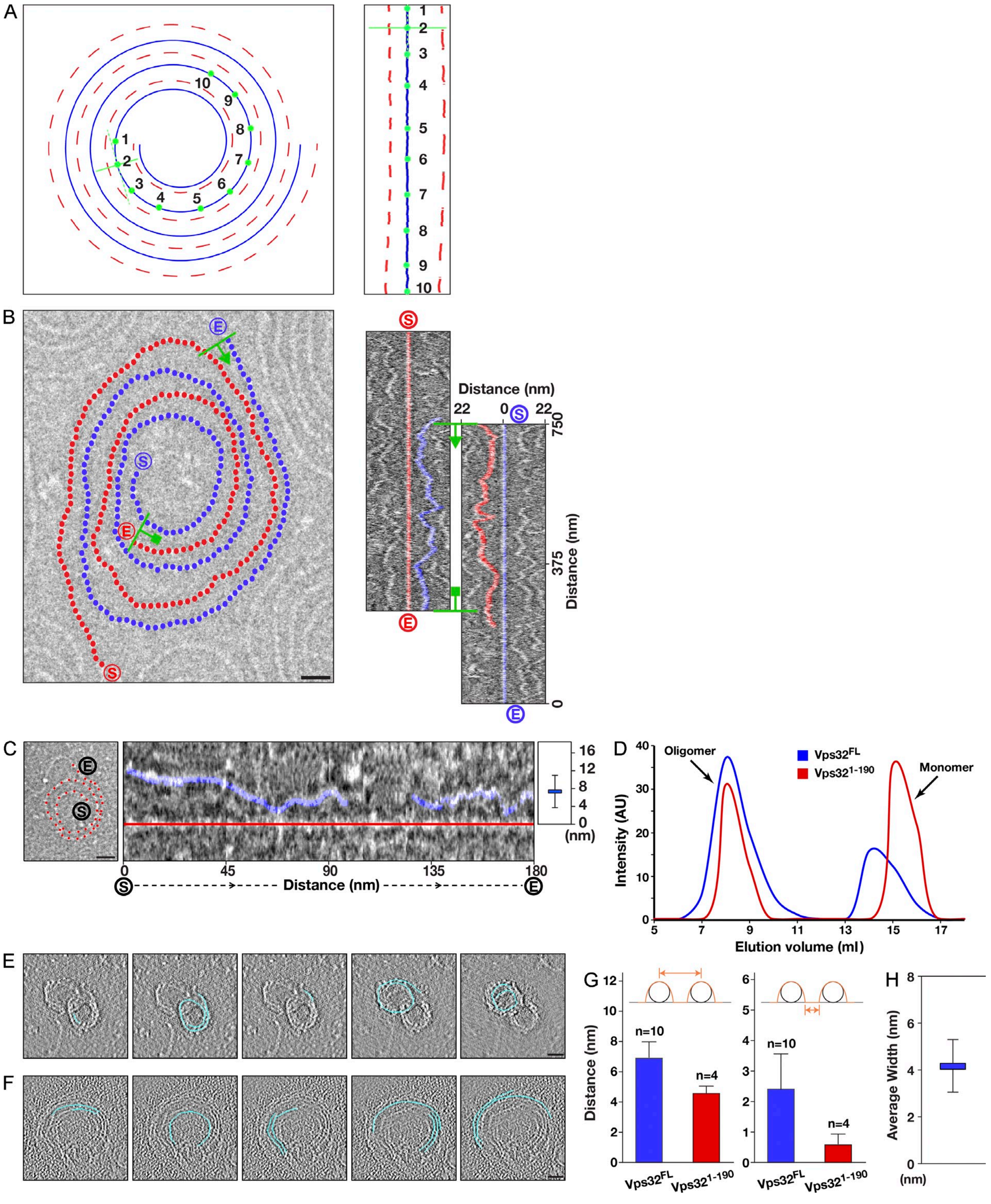

Figure S5. **The carboxyl terminus of Vps32 functions as a spacer between filaments within spirals.** (A) A filament-straightening tool was developed and used to determine the distance between the paths of two simulated spirals (a continuous blue spiral and a dashed red spiral). Accuracy was established by demonstrating that the distance calculated from individual points on one path (green) to juxtaposed dashed lines were identical before and after filament straightening. (B) The distance-measuring tool was used on an acquired image of two distinct, but entwined, Vps32 spirals. Two distinct filaments on the left were straightened, and the relative distance to of the adjacent filament was determined along its entire length. Axial symmetry in marked areas (green) further revealed the accuracy of the algorithm. The termini of each spiral are labeled (S [starting point] and E [ending point], color coded for each spiral). Bar, 10 nm. (C) Analysis of the spacing between filaments in negatively stained Vps32 spirals. (left) A representative negatively stained Vps32 spiral with its trajectory highlighted in red is shown. The ends of the spiral are indicated (S and E). Bar, 25 nm. (middle) A portion of this spiral was straightened, and its distance to the adjacent filament within the same structure was calculated along its entire length. (right) The average distance between the centers of each filament is plotted. Error bars represent means ± SEM. (D) A comparison of the elution profiles of wild-type Vps32 (FL, full length) and a truncated form of Vps32 (Vps32$^{1-190}$) after gel filtration chromatography indicates that both assemble as oligomers and monomers in solution. The data shown are from single representative experiments, which were repeated independently at least two times for each protein. AU, arbitrary unit. (E and F) The trajectories of the spirals composed of truncated Vps32 (Vps32$^{1-190}$) were derived from tomography datasets. The trajectories of filaments within the spirals are drawn (blue) at different tilting angles. Only distinct paths are shown at each tilting angle. (G) The distance between filaments within spirals composed of wild-type Vps32 (blue) and a truncated form of Vps32 (Vps32$^{1-190}$; red) was determined from the centers of each filament (left) or the edges of each filament (right). The differences in distances are statistically significant ($P < 0.01$, wild type compared with truncated Vps32, one-tail *t* test). Error bars represent means ± SEM. (H) Width analysis of Vps32$^{1-190}$ filaments (*n* = 15). Error bar represent means ± SEM.

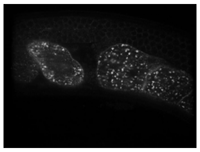

Video 1. **Caveolin transport during oocyte ovulation and early embryonic development.** *C. elegans* stably expressing GFP-caveolin (a cargo of the ESCRT-mediated degradation pathway) in the germline were imaged live by confocal microscopy using a swept-field confocal microscope (Ti-E; Nikon). The majority of GFP signal is lost before the two-cell stage as a result of ESCRT-mediated transport of caveolin into the lysosome lumen, as documented previously (Wang and Audhya, 2014). Frames were taken every minute for 153 min.

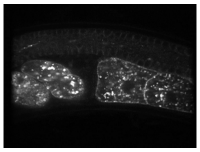

Video 2. **Caveolin degradation is impaired in embryos depleted of Vps32.** *C. elegans* stably expressing GFP-caveolin (a cargo of the ESCRT-mediated degradation pathway) in the germline were imaged live by confocal microscopy using a swept-field confocal microscope (Ti-E; Nikon) after RNA interference–mediated depletion of Vps32. The GFP signal is stabilized in developing embryos lacking Vps32 as a result of a defect in ESCRT-mediated trafficking of caveolin to the lysosome lumen. Frames were taken every minute for 123 min.

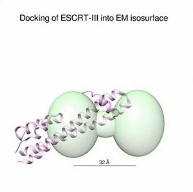

Video 3. **Docking of a Vps32 subunit onto the EM isosurface profile that was determined after two-dimensional class average analysis of Vps32 spiral filaments.** This video simulation shows several attempts to dock a pseudoatomic structure of a Vps32 monomer onto the EM isosurface determined by cryo-EM experiments of Vps32 filaments.

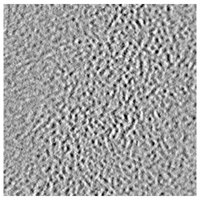

Video 4. **Tomogram of an individual spiral composed of truncated Vps32$^{1-190}$.** Samples of purified, negatively stained Vps32$^{1-190}$ were imaged by electron tomography using an FEI tomography holder with maximum tilt angles of ±60° (Tecnai G^2 F30; FEI). Each frame corresponds to a digital section of the tomogram moving along the tomographic z axis (1° increments).

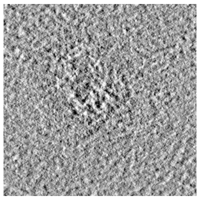

Video 5. **Tomogram of a spiral pair composed of truncated Vps32$^{1-190}$.** Samples of purified, negatively stained Vps32$^{1-190}$ were imaged by electron tomography using an FEI tomography holder with maximum tilt angles of ±60° (Tecnai G^2 F30; FEI). Each frame corresponds to a digital section of the tomogram moving along the tomographic z axis (1° increments).

A ZIP file is also provided that includes MATLAB scripts for particle picking, spiral interpolation, and spiral straighten developed for analysis of Vps32 filaments.

References

Muzioł, T., E. Pineda-Molina, R.B. Ravelli, A. Zamborlini, Y. Usami, H. Göttlinger, and W. Weissenhorn. 2006. Structural basis for budding by the ESCRT-III factor CHMP3. *Dev. Cell*. 10:821–830. http://dx.doi.org/10.1016/j.devcel.2006.03.013

Wang, L., and A. Audhya. 2014. In vivo imaging of *C. elegans* endocytosis. *Methods*. 68:518–528. http://dx.doi.org/10.1016/j.ymeth.2014.03.028